

# Chapter 4

## Diffuse Optical Tomography for Brain Imaging: Theory

Zhen Yuan and Huabei Jiang

### 4.1 Introduction

#### 4.1.1 *Recent Advances in Diffuse Optical Tomography*

Due to its numerous advantages including low cost, portability, and nonionizing radiation [1], near-infrared (NIR) diffuse optical tomography (DOT) is emerging as a potential tool for imaging biological tissues. To date, DOT has made a considerable advance and is being translated from the laboratory to the clinic. DOT is a natural extension of near-infrared spectroscopy (NIRS), which has been used clinically and in basic research, particularly in physiological and psychological research [2].

NIR light, with wavelengths between 600 and 1,000 nm, utilizes noninvasive radiation for imaging biological tissues. DOT using NIR light has been an active area of research for the past two decades. The main advantage of NIR DOT lies in providing a variety of quantitative information of biological tissues with high sensitivity and specificity compared to other imaging modalities. It has primarily been applied to image both structural and functional parameters of brain and breast tissues [3–7]. Recent phantom and clinical studies show that DOT can also provide quantitative optical images of hand joints and associated bones for early detection of joint-related diseases [8–11]. In addition, the potential use of molecular-specific contrast agents is an active research area with tremendous promise [12–14]. Presently, breast DOT can be performed repeatedly due to its nonionizing and noninvasive nature of imaging. Along with this, ongoing therapeutic investigations are showing a promise for monitoring chemotherapy using DOT [15–17].

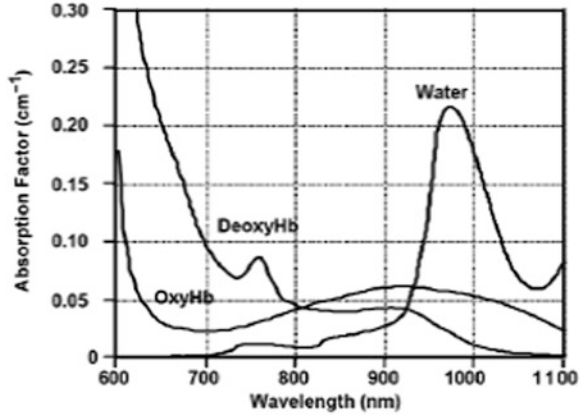
As a functional imaging modality, NIR DOT is appealing in terms of its intrinsic optical contrast due to hemoglobin in the blood which is the main absorber of NIR light in most tissues. Consequently, NIRS is capable of distinguishing oxy- and

---

Z. Yuan • H. Jiang (✉)

Department of Biomedical Engineering, University of Florida, Gainesville, FL 32611, USA  
e-mail: [hjiang@bme.ufl.edu](mailto:hjiang@bme.ufl.edu)

**Fig. 4.1** Absorption spectra of hemoglobin and water, showing a spectral window in tissues in the NIR region (<http://omlc.ogi.edu/spectra/>)



deoxy-hemoglobin, which then provides total hemoglobin (HbT) and blood oxygen saturation ( $SO_2$ ). In addition, tissue water and lipid contents can be estimated since there is a significant contribution of these contents to the NIR spectra. The distinct spectra for different chromophores make it possible to differentiate them in situ, which provides a powerful image-guided diffuse optical spectroscopy (DOS) technique for various applications including breast tissue imaging, brain functional imaging, finger joint imaging, molecular imaging, and photodynamic therapy monitoring [18–21] (Fig. 4.1).

DOT/DOS uses sophisticated image reconstruction techniques to generate images from multiple NIRS measurements. This generally involves solving both the forward problem and the inverse problem. In the forward problem, NIR light is delivered to the tissue surface and the transmitted and/or reflected light signal on the boundary is calculated based on the optical properties of tissue. Generally a diffusion model is used to approximate the propagation of NIR light in tissue. However, if the goal is to obtain the tissue property distribution from the measurement data, it is then defined as the inverse problem. With numerical methods, optimization algorithms, and regularization techniques, the distribution of the quantitative optical/physiological properties of tissue can be recovered using the assumed light transport model and measured boundary data [22–24].

Three typical signal measurement techniques using NIR light are currently being used for optical tissue imaging: continuous-wave (CW), time-domain (TD), and frequency-domain (FD) methods (Fig. 4.2) [19–21]. CW imaging systems directly measure the intensity of light transmitted and/or reflected through the tissue. The light source used in CW systems generally has a constant intensity or is modulated at a low frequency (a few kHz). TD systems use short laser pulses, with temporal spread below a nanosecond, and detect the increased spread of the pulse after passing through tissue. The time distribution of transmitted photons is known as the temporal point spread function (TPSF). By fitting the TPSF with a light propagation model such as the diffusion model, the medium parameters including absorption and scattering coefficients can be reconstructed. FD systems use an amplitude-modulated source at a high frequency (a few hundred MHz) and measure the attenuation of

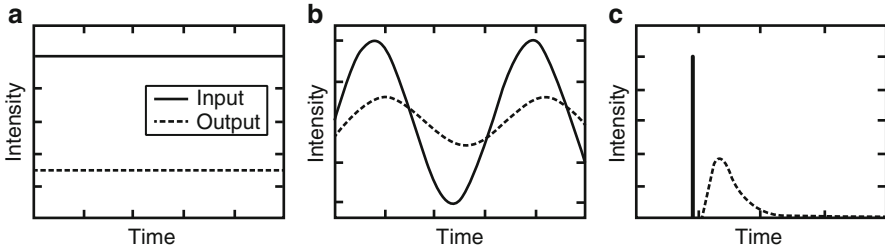


**Fig. 4.2** Measurement approach: (a) CW, (b) FD, (c) TD modes (*solid line*: input light source, *dashed line*: output detected signal)

amplitude and phase shift of the transmitted signal. Typically in this approach, a radio-frequency oscillator drives a laser diode and provides a reference signal for phase measurement. Among the three methods, the CW approach is relatively cheap and easy to implement; however, the absorption and scattering coefficients can be distinguished only with the use of appropriate regularization techniques or a prior information in reconstruction. The other two methods provide complete information about scattering events from transmitted photons in tissue, so that both absorption and scattering properties of tissue can be estimated effectively. Avalanche photodiodes are widely used in optical signal detection due to the high dynamic range. Photomultipliers provide higher sensitivity, although with a limited dynamic range and higher cost. Single photon counting PMTs are used in TD to measure the photon flight time. Recently charge-coupled devices (CCDs) are commonly used in CW systems for spectroscopic investigation to improve the imaging accuracy and reduce the data acquisition time.

However, the major limitation of DOT is its low spatial resolution due to the multiple scattering events that occur along each photon path. One effective way to improve its resolution is to integrate it with currently accepted high-resolution clinical imaging systems, such as mammography, ultrasound, X-ray computed tomography or tomography, and magnetic resonance [25]. As a consequence, NIR DOT has undergone a transition from a stand-alone imaging modality towards hybrid-modality combinations with standard clinical imaging systems. Other strategies to improve NIR imaging accuracy generally include: (1) Taking advantage of more spectral information in the NIR range; (2) using more accurate forward model or robust reconstruction method; (3) building a reliable imaging system with high sensitivity and specificity; (4) using contrast agents to improve the imaging sensitivity and specificity. For example, the use of a priori spatial and spectroscopic information has been reported to achieve high-resolution DOT imaging with NIRS [21, 26].

### 4.1.2 Recent Advances in Neuroimaging Using DOT

Compared to other functional imaging modalities, such as functional magnetic resonance imaging (fMRI) and PET, DOT has the advantages of noninvasive, portable, convenience, and low cost, and, more importantly, it has unsurpassed

high temporal resolution, which is essential for revealing rapid change of dynamic patterns of brain activities including change of blood oxygen, blood volume, and blood flow.

Since the mid-1990, most of the research work done in neuroscience using optical measurements has been focused on NIR spectroscopy or imaging of human and small animal brain function. They have utilized these optical techniques to localize or monitor the cerebral responses under different stimulus including visual [27–29], auditory [30], somatosensory [31], motor [32–34] and language [35]. Further, the researchers also investigated the neurological disorders using different measurement instrumentations and attempted to address neurovascular and neurometabolic coupling mechanisms for different diseases, such as seizure and epilepsy [36–39], depression [40–42], Alzheimer [43–45], and stroke rehabilitation [46–49]. In particular, most of the imaging work conducted was implemented with a sparse array, in which the sources and detectors were separated between 2 and 4 cm, providing low sensitivity and low spatial resolution [50]. Generally speaking, this is not DOT and has been termed optical topography (OT). So far most of the developed reconstruction methods in OT are limited to linear algorithms, which can only provide the change of optical or physiological properties of biological tissues with limited spatial resolution.

In contrast, DOT is generally implemented with a relatively dense array, which provides source and detector pairs with a number of separations [51]. The pairs that are close together will be more sensitive to superficial tissues (e.g., scalp, skull), whereas the pairs with a greater separation will be more sensitive to deeper tissues (e.g., cortex). As such, overlapping information from multiple detector pairs can be combined in the form of a model-based 3D image reconstruction. Reconstructing data can improve depth sensitivity and decrease physiological noise. Recent studies have demonstrated much higher resolution mapping of certain areas in the cortex using nonlinear or linear DOT reconstruction algorithms [52–54].

So far DOT is a relatively new addition to the field of functional neuroimaging, and there is little standardization. There is a growing effort within the optical imaging community to develop a more systematic framework for experimental design and data analysis. Additionally, multimodal imaging combining DOT with the existing brain imaging techniques in synergistic ways facilitates improved interpretation of data and provides brain functional map with excellent temporal and spatial resolution. In particular, MRI- or CT-guided DOT should have tremendous competitive power in future, which can provide 3D DOT of the whole brain based on the realistic head model.

## 4.2 Image Reconstruction Methods in DOT

In early days, OT reconstruction methods tried to recover the change in optical/physiological properties using the measured change in intensity. The spatial resolution provided by OT could not be better than the spacing between the sources and

detectors [2]. One of the most significant improvements in image quality in OT came when a forward model was set up, which describes the geometry and the baseline optical properties of the head, and was used to calculate the amount by which each measurement would change given a small change in optical properties of each pixel. These values were assembled into a sensitivity matrix, which was then inverted and multiplied by the measured data to give an image. This process is not straightforward, as the sensitivity matrix is ill-posed and underdetermined [56–58]. In these OT reconstruction methods, linear algorithms are utilized and the sources and detectors are separated between 2 and 4 cm, providing low sensitivity and low spatial resolution.

DOT reconstruction algorithms allow multiple measurements to contribute to each pixel, leading to improvements in spatial resolution, and accuracy of quantitative tissue parameter reconstruction up to a factor of two [51, 59]. Various reconstruction schemes have been developed for DOT, such as analytical, back-projection, and linear and nonlinear methods. However, in this community regularization-based nonlinear methods have gained the highest attention since they can achieve highly accurate and quantitative image reconstruction. In the following sections, we focus on the description of the basic principles in nonlinear DOT reconstruction methods including the forward problem, the inverse problem, multi-modality imaging approach, spectral reconstruction, and vascular parameter recoveries.

### 4.2.1 Forward Problem

The development of a model to describe light migration in tissue is essential for the assessment of measurements in diagnostic NIRS and DOT. The equation of radiation transport (RTE) has been accepted as an accurate model to describe light migration in scattering media such as tissue [60, 61]. However, the RTE is difficult to solve, even in homogeneous media with simple boundaries. Additionally, solving the inverse problem with RTE is an even more daunting and time-consuming task. Present modeling of light propagation in scattering tissues is largely through the utilization of the diffusion approximation to the radiation transport equation, i.e., the photon diffuse equation which has the following form in the TD:

$$\nabla \cdot D(r)\nabla\Phi(r, t) - \mu_a(r)\Phi(r, t) - \frac{\partial\Phi(r, t)}{v\partial t} = -S(r, t) \quad (4.1)$$

in which  $r$  is the position vector (mm),  $t$  is the time (s),  $v$  is the speed of light in the medium (mm/s),  $\Phi(r, t)$  is the photon density (photon fluence rate:  $\text{mW}/\text{mm}^2$ ),  $D(r)$  the diffusion coefficient ( $\text{mm}^{-1}$ ),  $\mu_a(r)$  is the optical absorption coefficient ( $\text{mm}^{-1}$ ),  $S(r, t)$  is the source strength ( $\text{mW}/\text{mm}^3$ ), and the diffusion coefficient can be written as  $D = 1/(3(\mu_a + \mu'_s))$ , where  $\mu'_s$  is the reduced scattering coefficients ( $\text{mm}^{-1}$ ). Typically, the source is modeled as a single isotropic point source placed  $1/\mu'_s$  (1 mm) into the medium. The photon density near the boundary of turbid

medium/tissue is generally described by the mixed Dirichlet–Neuman boundary condition (Type-III Boundary conditions) [24]:

$$D\nabla\Phi(r, t) \cdot \hat{n} = -\alpha\Phi(r, t) \quad (4.2)$$

in which  $\hat{n}$  is the vector normal to measurement boundary,  $\alpha$  is related to the refractive index ( $n$ ) mismatch at the boundary via the following expression:  $\alpha = \frac{1-R_{\text{eff}}}{R_{\text{eff}}} \frac{3}{2} \mu'_s$ ,  $R_{\text{eff}} \approx \frac{-1.44}{n^2} + \frac{0.71}{n} + 0.668 + 0.63n$  and  $n = \frac{n_{\text{in}}}{n_{\text{out}}}$ .

The FD diffusion equation is obtained through the Fourier transform of (4.1):

$$\nabla \cdot D(r)\nabla\Phi(r, \omega) - \left( \mu_a(r) + \frac{i\omega}{c} \right) \Phi(r, \omega) = -S(r, \omega) \quad (4.3)$$

In FD, we have assumed that  $\Phi(r, t) = \Phi(r)e^{-i\omega t}$ , and the  $e^{-i\omega t}$  terms have been factored out, since the detected signals are modulated at the same frequency as the light source ( $\omega$ : light source modulation frequency). For a CW case where  $\omega = 0$ , the following photon diffusion equation and type-III boundary condition are derived,

$$\nabla \cdot D(r)\nabla\Phi(r) - \mu_a(r)\Phi(r) = -S(r) \quad (4.4)$$

$$-D\nabla\Phi \cdot n = \alpha\Phi \quad (4.5)$$

The finite element (FE) method is the most widely used numerical method to solve the photon diffusion equation. To solve (4.4) and (4.5) using FE (a similar operation can be implemented for FD and TD cases), the weighted weak form for these two equations is stated as

$$\int_V \phi_i(\nabla \cdot D(r)\nabla\Phi - \mu_a\Phi + S) dV + \int_\Gamma \phi_i(-D\nabla\Phi \cdot n - \alpha\Phi) d\Gamma = 0 \quad (4.6)$$

According to integration by parts, (4.6) is rewritten as follows:

$$\int_V (D(r)\nabla\phi_i \cdot \nabla\Phi(r) + \mu_a\phi_i\Phi(r) - \phi_i S) dV + \int_\Gamma \phi_i(\alpha\Phi) d\Gamma = 0 \quad (4.7)$$

In addition,  $\Phi(r)$ ,  $D$  and  $\mu_a$  are spatially discretized as

$$\Phi = \sum_{i=1}^N \Phi_i \phi_i, \quad D = \sum_{i=1}^N D_i \phi_i, \quad \mu_a = \sum_{i=1}^N (\mu_a)_i \phi_i \quad (4.8)$$

in which  $N$  is the node number of the finite element mesh and  $\phi_i$  is the basis function. In consideration of (4.8), (4.7) can be written as

$$[A]\{\Phi\} = \{b\} \quad (4.9)$$

in which the elements of the matrix  $[A]$  are  $\alpha_{ij} = \int_V (-D\nabla\phi_j \cdot \nabla\phi_i - \mu_a\phi_j\phi_i) dV + \int_\Gamma (-\alpha\phi_j\phi_i) d\Gamma$  where the integrations are performed over the problem domain ( $V$ ) and boundary domain ( $\Gamma$ ).  $\{b\}$  is the source vector. Assuming a point source model,  $S = S_0\delta(r - r_0)$  is used, where  $S_0$  is the source strength and  $\delta(r - r_0)$  is the Dirac delta function for a source at  $r_0$ .

### 4.2.2 Inverse Problem: Problem Statement for Nonlinear Reconstruction Methods

In solving the inverse problem for DOT, the goal is to recover the optical properties at each FE node using a finite number of measurements at the tissue surface. The objective function for regularized minimization statement is given [62] as follows:

$$\mathbf{F} = \min_{\chi} \left\{ \sum_{i=1}^M (\Phi_i^m - \Phi_i^c)^2 + \eta \|\chi - \chi_0\|^2 \right\} \quad (4.10)$$

in which  $\chi$  expresses  $D$  and  $\mu_a$ ,  $\chi_0$  is usually fixed,  $\Phi_i^m$  is the measured photon density from a given scattering medium for  $i = 1, 2, \dots, M$  boundary locations, and  $\Phi_i^c$  is the computed photon density with the same geometry as the scattering medium. In nonlinear and iterative-based reconstruction algorithms,  $\chi_0$  is set equal to  $\chi_i$  determined by the recovered parameters at the previous iteration. This variation is termed the Levenberg–Marquardt algorithm [63, 64]. In this case, (4.10) is further simplified to

$$\text{Min: } F = \sum_{i=1}^M (\Phi_i^m - \Phi_i^c)^2 \quad (4.11)$$

We can minimize the objective function by specifying  $F = 0$ . This is a typical optimization problem, where we are particularly interested in finding  $\chi$  that makes  $F$  close to zero. Following a Taylor series expansion method, we obtain the approximated  $\chi$  from nearby point  $\chi_0$  ( $\Delta\chi = \chi - \chi_0$ ),

$$\frac{\partial F}{\partial \chi} = \frac{\partial F}{\partial \chi}(\chi_0) + \Delta\chi \frac{d}{d\chi} \left[ \frac{\partial F}{\partial \chi}(\chi_0) \right] + \dots \quad (4.12)$$

If the effect of the higher-order terms is ignored and  $\partial F/\partial\chi = 0$  is assumed, (4.12) is rewritten as follows:

$$\chi = \chi_0 - \left\{ \frac{d}{d\chi} \left[ \frac{\partial F}{\partial\chi}(\chi_0) \right] \right\}^{-1} \frac{\partial F}{\partial\chi}(\chi_0) \quad (4.13)$$

The iterative form for (4.13) can be specified as

$$\chi_i = \chi_{i-1} - \left\{ \frac{d}{d\chi} \left[ \frac{\partial F}{\partial\chi}(\chi_{i-1}) \right] \right\}^{-1} \frac{\partial F}{\partial\chi}(\chi_{i-1}) \quad (4.14)$$

Based on (4.11), we can solve for the first-order and second-order derivatives of  $F$

$$\frac{\partial F}{\partial\chi} = 2 \left( \frac{\partial\Phi^c}{\partial\chi} \right)^T (\Phi^c - \Phi^m) \quad (4.15)$$

$$\frac{\partial^2 F}{\partial\chi^2} = 2 \left( \frac{\partial\Phi^c}{\partial\chi} \right)^T \frac{\partial\Phi^c}{\partial\chi} + 2 \left( \frac{\partial^2\Phi^c}{\partial\chi^2} \right)^T (\Phi^c - \Phi^m) \quad (4.16)$$

The contribution from the higher-order derivative terms in (4.16) is small and often discarded. Then inserting (4.16) into (4.14), we get

$$\chi_i = \chi_{i-1} + \left\{ 2 \left( \frac{\partial\Phi^c}{\partial\chi} \right)^T \frac{\partial\Phi^c}{\partial\chi} \right\}^{-1} 2 \left( \frac{\partial\Phi^c}{\partial\chi} \right)^T (\Phi^m - \Phi^c) \quad (4.17)$$

in which  $\partial\Phi/\partial\chi$  is the Jacobian matrix  $J$ , formed at the boundary measurement sites. It should be noted that the impact of the Hessian matrix  $J^T J$  in (4.17) is always ill-conditioned, which makes the iteration process unstable. A typical way to stabilize the inversion problem is through regularization to make  $J^T J$  more diagonally dominant. So the ultimate iterative updating equation for the optical properties in (4.17) becomes

$$(J^T J + \lambda' \mathbf{I}) \Delta\chi = J^T (\Phi^m - \Phi^c) \quad (4.18)$$

in which,  $\lambda'$  is a scalar and  $\mathbf{I}$  is the identity matrix. A very effective method for determining  $\lambda'$  is to set it equal to the trace of the Hessian matrix multiplied by an empirically determined factor  $\sigma$ , and the least-square error at each iteration,

$$\lambda' = \sigma (\Phi^c - \Phi^m)^2 \times \text{trace}[J^T J] \quad (4.19)$$



Moreover, the adjoint sensitivity method is often implemented to calculate the Jacobian matrix, which is able to reduce the computational cost dramatically. Direct differentiation of both sides of (4.9) with respect to  $\chi$

$$[A] \left\{ \frac{\partial \Phi}{\partial \chi} \right\} = - \left[ \frac{\partial A}{\partial \chi} \right] \{ \Phi \} \quad (4.20)$$

The Jacobian matrix  $\partial \Phi / \partial \chi$  can be calculated through the following steps.

First, we define a  $N$  (node number)  $\times$   $M$  (measurement number) matrix  $\Psi$ , and let  $\Psi$  satisfy the following relationship:

$$[A]^T [\Psi] = [\Delta_d] \quad (4.21)$$

where the vector  $\Delta_d$  has the unit value at the measurement sites/nodes and zero at other nodes. Then we left multiply (4.20) with the transposition of  $[\Psi]$

$$[\Psi]^T [A] \left\{ \frac{\partial \Phi}{\partial \chi} \right\} = - [\Psi]^T \left[ \frac{\partial A}{\partial \chi} \right] \{ \Phi \} \quad (4.22)$$

Equation (4.22) can be further written as follows:

$$\left\{ \frac{\partial \Phi}{\partial \chi} \right\}^T [A]^T [\Psi] = - \{ \Phi \}^T \left[ \frac{\partial A}{\partial \chi} \right]^T [\Psi] \quad (4.23)$$

Inspecting (4.21) into (4.23), we get

$$\left\{ \frac{\partial \Phi}{\partial \chi} \right\}^T = - \{ \Phi \}^T \left[ \frac{\partial A}{\partial \chi} \right]^T [\Psi] \quad (4.24)$$

Now we can immediately tell that the left-hand side of the above equations actually gives the corresponding elements in the relative Jacobian matrix based on the adjoint sensitivity method

$$\left\{ \frac{\partial \Phi}{\partial \chi} \right\} = - [\Psi]^T \left[ \frac{\partial A}{\partial \chi} \right] \{ \Phi \} \quad (4.25)$$

The nonlinear reconstruction approach described so far is an iterative Newton method with combined Marquardt and Tikhonov regularizations that can provide stable inverse solutions. The Newton reconstruction process involves the iterative solution of the above equations (4.9) and (4.18), allowing an update of optical property distribution to be obtained at each iteration, i.e.,  $\chi_{\text{new}} = \chi_{\text{old}} + \Delta \chi$ . However, to improve the reconstruction accuracy, the global convergence-based Newton method is often used using the following modified updating procedure [11]:

$$\chi_{\text{new}} = \chi_{\text{old}} + \zeta \Delta \chi \quad (0 < \zeta \leq 1) \quad (4.26)$$

where  $\zeta$  is calculated from a backtracking line search. Thus the realization of the global convergence algorithm is quite straightforward: the algorithm starts with a full Newton step (i.e.,  $\zeta = 1$ ); if the updated  $\chi$  are close enough to the final solution, a quadratic convergence is obtained; if not, the backtracking line search will provide a smaller value of  $\zeta$  along the Newton direction; the reconstruction process continues until a quadratic convergence is achieved.

Finally, high quality image reconstruction based on the above iterative procedure depends on good choice of four initial parameters including the BC coefficient  $\alpha$ , the source strength  $S$ , and the initial guesses of  $D$  and  $\mu_s$ . As such, an optimization scheme was developed to find the best initial guesses based on the forward computation of the diffusion equation so that the following objective function is minimized [22]:

$$\text{Min: } \pi = \sum_{i=1}^M (\Phi_i^m - \Phi_i^c \text{ (calculated from optimized initial guesses)}) \quad (4.27)$$

in which  $\Phi_i^m$  is the measured photon density from a given experimental inhomogeneous medium, and  $\Phi_i^c$  is the computed photon density from a homogeneous medium with the same geometry as the experimental medium.

### 4.2.3 Multi-Modality Image Reconstruction Method

It is widely accepted that DOT can provide high-contrast biological tissue imaging with quantitative optical properties. However, the limitation of tomographic NIRS and DOT is their low resolution due to the multi-scattering events that occur along each photon path. As mentioned in Sect. 4.1.2, an effective way to enhance its resolution is to integrate it with the existing high-resolution clinical imaging systems, such as mammography, ultrasound (US), X-ray computed tomography (CT) or tomosynthesis, and magnetic resonance (MR) [25].

While several methods are available in the area of high-resolution imaging modality-guided DOT reconstruction [5, 65–69], regularization-based schemes appear to be the most effective as they can flexibly handle the problems associated with incorrect initial estimation of optical properties and inaccurate domain segmentation that are required for a priori structural information guided DOT reconstruction. Several regularization-based schemes have been developed for high-resolution imaging (MR, US, and CT) guided DOT reconstruction. However, most of these schemes do not appear to be able to handle the cases where MR or CT is insensitive to the target tissues or lesions, resulting in inaccurate DOT reconstruction. To overcome these limitations, a modified Tikhonov or hybrid regularization technique has been conducted for spatial information guided DOT reconstruction [70].

The conventional Tikhonov-regularization sets up a weighted term as well as a penalty term to minimize the squared differences between computed and measured photon density values as follows:

$$\min_{\chi} : \{ \|\Phi^c - \Phi^o\|^2 + \rho \|\mathbf{L}\delta\chi\|^2 = \{ \|\Phi^c - \Phi^o\|^2 + \rho \|\mathbf{L}(\chi^c - \chi^o)\|^2 \} \quad (4.28)$$

And the generated updating equation based on Newton iterative method can be expressed as

$$\Delta\chi = (J^T J + \rho \mathbf{L}^T \mathbf{L})^{-1} [J^T (\Phi^o - \Phi^c) - \rho \mathbf{L}^T \mathbf{L} \chi] \quad (4.29)$$

in which  $\Phi^o = (\Phi_1^o, \Phi_2^o, \dots, \Phi_M^o)^T$  and  $\Phi^c = (\Phi_1^c, \Phi_2^c, \dots, \Phi_M^c)^T$ , and  $\Phi_i^o$  and  $\Phi_i^c$  are observed and computed photon intensity for  $i = 1, 2, \dots, M$  boundary locations;  $\rho$  is the weighted parameter;  $\mathbf{L}$  is the regularization matrix or filter matrix.

In consideration of the fact that Tikhonov regularization can draw the solution towards the null space of the regularization matrix  $\mathbf{L}$ , that is  $\mathbf{L}\chi^0 = 0$ , we obtain the following updating equation when  $\rho = 1$ ,

$$\Delta\chi = (J^T J + \mathbf{L}^T \mathbf{L})^{-1} [J^T (\Phi^o - \Phi^c)] \quad (4.30)$$

The most often used regularization matrices in DOT are the identity, in which  $\mathbf{L}$  is a diagonal matrix and the prior information can be incorporated into the iterative process by using the spatially variant regularization parameter [67, 68]. The Laplacian-type filter matrix  $\mathbf{L}$  is often used and its elements,  $L_{ij}$  are constructed according to the visible region or tissue type it was associated as follows [65]:

$$L_{ij} = \begin{cases} 1 & \text{if } i = j \\ -1/NN & \text{if } i, j \subset \text{one region} \\ 0 & \text{if } i, j \subset \text{different region} \end{cases} \quad (4.31)$$

where  $NN$  is the finite element node number within a tissue type.

However, the multi-modality imaging schemes expressed in (4.30) are not able to handle the cases where MR or X-ray is insensitive to the target tissues or lesions. For example, in the area of joint imaging, X-ray is not able to detect the cartilage and fluids as well as their changes in the finger joints, although the changes associated with the cartilage and fluids can be easily captured by low-resolution DOT alone. To resolve this issue, instead of imposing constraints on the magnitude of the solution or on its derivative as in Tikhonov regularization, the developed hybrid regularization method minimizes the difference between the desired solution and its approximate X-ray or MR estimate, as well as the residual error in the least square sense. Hence in hybrid regularization-based nonlinear reconstruction algorithm, the objective function becomes

$$\min_{\chi} : \|\Phi^c - \Phi^o\|^2 + \beta \left\{ \|\Phi^c - \Phi^o\|^2 + \lambda \|\mathbf{L}\delta\chi\|^2 \right\} \quad (4.32)$$

where  $\beta$  is the hybrid regularization parameter. By minimizing  $\Omega$  with respect to  $\chi$  (i.e.,  $\partial\Omega/\partial\chi = 0$ ) and considering (4.30), we obtain the following updating equation for the hybrid regularization:

$$\Delta\chi = (J^T J + \beta J^T J + \lambda' I + \beta \mathbf{L}^T \mathbf{L})^{-1} [J^T (\Phi^o - \Phi^c)] \quad (4.33)$$

If we specify the regularization parameter  $\beta = 1$ , (4.6) is further simplified as

$$\Delta\chi = (J^T J + J^T J + \lambda' I + \mathbf{L}^T \mathbf{L})^{-1} [J^T (\Phi^o - \Phi^c)] \quad (4.34)$$

in which  $\lambda'$  is the Levenberg–Marquardt regularization parameter. It is noted from (4.34) that the hybrid regularization is actually a regularization scheme that combines both Levenberg–Marquardt and Tikhonov-regularization.

#### 4.2.4 Diffuse Optical Spectral Reconstruction of Physiological Parameters of Tissues

DOS and DOT have more than 30-year history of being used to access tissue spectral parameters including HbT concentration, hemoglobin oxygen saturation, water and lipid concentration, scattering amplitude, and scattering power. Early work in the field of tomographic DOS focused on reconstruction of optical properties of tissue at several selected wavelengths. Then a least-square fitting algorithm was utilized to estimate the chromophore concentrations based on the recovered optical properties and Beer's Law [20, 71]. To date several methods are proposed to directly image the chromophore concentrations without first estimating the optical properties either in CW- or frequency-domain [26, 72]. An interesting study has shown that oxyhemoglobin ( $\text{HbO}_2$ ), deoxyhemoglobin (Hb), water and scattering amplitude heterogeneities could be successfully recovered using CW measurements at four optimized wavelengths in the 650–930 nm range [73]. In particular, the use of a priori spatial and spectroscopic information has been reported to achieve high-resolution DOT imaging with NIRS [21, 26]. Chromophore concentrations can be reconstructed with high accuracy when spatial guidance from high-resolution imaging methods and spectral a priori information provided by NIRS are used [21, 26].

When the data acquisition at different wavelengths is finished, the following step is to generate the spectroscopic images based on a robust 3D reconstruction algorithm. For the forward problem, the photon density at different wavelengths can be calculated from the photon diffusion model using the finite element method. For CW cases, the spectra resolved forward model is written (similar operation can be conducted for FD and TD cases):

$$\nabla \cdot D(r, \lambda) \nabla \Phi(r, \lambda) - \mu_a(r, \lambda) \Phi(r, \lambda) = -S(r, \lambda) \quad (4.35)$$

According to Beer's law, the wavelength-dependent tissue absorption is

$$\mu_a(\lambda) = \sum_{i=1} \varepsilon_i(\lambda) c_i \quad (4.36)$$

in which  $c_i$  is the concentration,  $\varepsilon_i(\lambda)$  is the extinction absorption coefficient of the  $i$ th chromophore (HbO<sub>2</sub>, Hb, H<sub>2</sub>O and lipid) at wavelength  $\lambda$ . Scattering properties (scattering amplitude  $a$  and scattering power  $b$ ) are found by constructing a best fit to an empirical approximation to Mie scattering theory,

$$\mu'_s = a\lambda^{-b} \quad (4.37)$$

Thus the forward model is further written as follows:

$$\nabla \cdot D \nabla \Phi(r, \lambda) - \sum_{i=1} \varepsilon_i(\lambda) c_i \Phi(r, \lambda) = -S(r, \lambda) \quad (4.38)$$

For the inverse problem, the following updating equation for the hybrid regularization is deduced [21],

$$\Delta \chi_\lambda = (J^T J + J^T J + \lambda' \mathbf{I} + \mathbf{L}^T \mathbf{L})^{-1} [J^T (\Phi^o(\lambda) - \Phi^c(\lambda))] \quad (4.39)$$

If no spatial guidance is incorporated, (4.39) is reduced to

$$\Delta \chi_\lambda = (J^T J + \lambda' \mathbf{I})^{-1} [J^T (\Phi^o(\lambda) - \Phi^c(\lambda))] \quad (4.40)$$

where  $\Delta \chi_\lambda = ([\Delta c_1] \ \cdots \ [\Delta c_n] \ [\Delta a] \ [\Delta b])^T$  is the updating vectors for the absorbers and scatters. The Jacobian matrix  $\mathbf{J}$  is denoted:  $\mathbf{J} = [\tilde{J}_{1,\lambda}, \dots, \tilde{J}_{c,\lambda}, \tilde{J}_{a,\lambda}, \tilde{J}_{b,\lambda}]$ , where  $\tilde{J}_{c,\lambda}$  represent the Jacobian submatrices for different chromophores and is stated:

$$\tilde{J}_{c,\lambda} = \frac{\partial \Phi(\lambda)}{\partial \mu_a} \frac{\partial \mu_a}{\partial c_i} \quad (4.41)$$

When  $D(\lambda)$  is expressed in terms of  $a$  and  $b$  using (4.37), the other Jacobian submatrices are written in consideration of  $D = 1/(3(\mu_a + \mu'_s))$

$$\tilde{J}_{a,\lambda} = \frac{\partial \Phi(\lambda)}{\partial D} (-3D^2 \lambda^{-b}), \quad \tilde{J}_{b,\lambda} = \frac{\partial \Phi(\lambda)}{\partial D} (3D^2 \mu'_s \ln \lambda) \quad (4.42)$$

Thus the image formation task for the spectral reconstruction is to update an optimized initial chromophore concentration distribution via iterative solution of (4.38) and (4.39) so that a weighted sum of the squared difference between the computed  $\Phi^c(\lambda)$  and measured photon density  $\Phi^o(\lambda)$  in (4.43) can be minimized:

$$\Omega = \|\Phi^c(\lambda) - \Phi^o(\lambda)\|^2 \quad (4.43)$$

#### ***4.2.5 Calculation of Vascular Parameters (Cerebral Blood Flow Rate and Oxygen Consumption Rate) Based on the Recovered Physiological Responses***

Analysis of the physiological responses of functional brain activation based on intrinsic signals has revealed new insights into the functional representations of areas such as the visual and somatosensory cortices [74, 75]. In addition to hemoglobin change, cerebral blood flow (CBF) and oxygen consumption rate (OC) changes resulting from functional activation are also important components of the hemodynamic response. Coupling between neuronal activity and the associated hemodynamic response is now becoming a hot topic in neuroscience [76, 77]. A clearer understanding of the neuro–metabolic–vascular relationship will enable greater insight into the functioning of the normal brain and will also have significant impact on diagnosis and treatment of neurovascular diseases such as stroke, Alzheimer’s disease, brain injury, and epilepsy [78]. In order to achieve this goal, simultaneous monitoring of the spatiotemporal characteristics of OC, CBF, and the cerebral metabolic rate of oxygen is crucial.

Although numerous methods for assessment of cerebral OC and CBF have been explored including fMRI [79], arterial spin labeling MRI [80], PET [81], Fick’s law-based optical systems [82], laser Doppler [83], diffuse correlation spectroscopy [84], and Doppler ultrasound [85], there remains a critical need for continuous, noninvasive instruments to measure CBF and OC in humans with intact skull. For example, the spatiotemporal resolution of PET is limited, and fMRI requires careful calibration of the scaling factor between the blood oxygen level-dependent signal and the relative changes of Hb concentration, as well as assumptions about the relationship between the changes in CBF and cerebral blood volume. Laser Doppler flow meter has limited penetration depth. Diffuse correlation spectroscopy has shown promising results, but it is still unclear whether it is practical enough to be used for continuous monitoring in humans. Fick’s law-based systems are not entirely noninvasive, since they require the injection of a chromophore, and therefore cannot be used for continuous monitoring [86]. Laser speckle contrast imaging method can effectively recover the BF and OC parameters, but it is limited to superficial imaging [75].

NIR DOS and DOT have shown great potential to provide high spatiotemporal resolution and quantitative imaging of hemodynamic responses. In particular, dynamic optical imaging has allowed the exploration of time-resolved changes in tissue properties. The cerebral functional dynamics measured by DOT are due to the dynamical changes in blood volume and oxygenation in the scalp and brain where the hemodynamics are caused by CBF and OC change associated with heart beat, vasomotion, and vascular response to neuronal activity [87]. However, current dynamic DOT imaging techniques provide only the change of HbT and SO<sub>2</sub>, which cannot give the change of CBF and OC due to the hemodynamic response to

neuronal activation. As such, new mathematical models connecting changes in CBF and OC to observed changes in HbT and  $\text{SO}_2$  are required to guide more quantitative interpretation of neuronal activity. The model should be able to provide indirect measurements of neuron-induced vascular parameters including blood flow rate (BF) and OC.

The principle of mass balance to the transport of oxygen in a blood vessel segment allows us to obtain quantitative information on how oxygen and blood are managed in tissue. To model oxygen transport in a blood vessel by this principle, we consider a one-dimensional cylindrical vessel (blood vessel) with  $R_i$  and  $R_o$  as the inner and outer radii, respectively, surrounded by other biological tissues. In addition, we assume all the oxygen ( $\text{O}_2$ ) diffusing out the segment is consumed in a surrounding tissue region [88].

#### 4.2.5.1 Mass Balance in Each Segment for Intravascular Flux

The law of mass conservation stipulates that the amount of  $\text{O}_2$  lost from a vascular segment must be equal to the diffuse  $\text{O}_2$  flux to the tissues, determined by the perivascular oxygen gradients. For a steady case, we have

$$Q_{\text{in}}C_b[\text{HbT}]\text{SO}_{2,\text{in}} - Q_{\text{out}}C_b[\text{HbT}]\text{SO}_{2,\text{out}} = l_i\pi d_i J_i \quad (4.44)$$

in which  $Q_{\text{in}}$  (mL/s) is the volumetric BF into the  $i$ th segment,  $Q_{\text{out}}$  the volumetric BF out of the segment,  $d_i$  is the diameter of the  $i$ th segment,  $l_i$  the length of the  $i$ th segment, HbT the total hemoglobin concentration in the blood (moles/mL),  $\text{SO}_{2,\text{in}}$  the hemoglobin oxygen saturation flowing in the segment,  $\text{SO}_{2,\text{out}}$  oxygen saturation flowing out of the segment,  $J_i$  the oxygen flux across the vessel wall (moles  $\text{O}_2/\text{cm}^2/\text{s}$ ), and  $C_b$  is the oxygen binding capability of hemoglobin ( $C_b = 1.39$  mL  $\text{O}_2/\text{gmHb}$ ;  $C_b = 1$ . if the concentration of  $\text{O}_2$  dissolved in plasma is considered) [88]. In addition, (4.44) is rewritten in consideration of the mean BF:

$$Q_i C_b [\text{HbT}] (\text{SO}_{2,\text{in}} - \text{SO}_{2,\text{out}}) = l_i \pi d_i J_i \quad (4.45)$$

where  $Q_i$  is the mean BF in the  $i$ th segment. For a transient case, (4.44) is further written as follows:

$$Q_{\text{in}}(t)C_b[\text{HbT}]\text{SO}_{2,\text{in}}(t) - Q_{\text{out}}(t)C_b[\text{HbT}]\text{SO}_{2,\text{out}}(t) - l_i\pi d_i J_i(t) = \frac{\partial M_{i,\text{HbO}_2}(t)}{\partial t} \quad (4.46)$$

in which  $M_{i,\text{HbO}_2}$  is the moles of oxygenated hemoglobin in the  $i$ th segment. According to the principle of mass balance, the third term on the left-hand side of (4.46) is actually the  $\text{OC}_i$  of the  $i$ th segment (mole  $\text{O}_2/\text{s}$ ). Considering the fact that

each molecule of hemoglobin is able to carry four molecules of oxygen, (4.46) is stated as follows:

$$\begin{aligned} Q_{\text{in}}(t)C_b[\text{HbT}]\text{SO}_{2,\text{in}}(t) - Q_{\text{out}}(t)C_b[\text{HbT}]\text{SO}_{2,\text{out}}(t) \\ - \text{OC}_i(t)/4 = \frac{\partial M_{i,\text{HbO}_2}(t)}{\partial t} \end{aligned} \quad (4.47)$$

#### 4.2.5.2 Mass Balance in Tissues Based on Global Analysis for Estimating Intravascular Flux

The oxygen consumed by the tissues (organs) is supplied from three blood vessel sources: capillaries, arterioles, and venules. As such, mass balance for  $\text{O}_2$  in the whole tissues (organ) yields for a steady case

$$\sum_{i=1}^M (Q_{\text{in}}C_b[\text{HbT}]\text{SO}_{2,\text{in}} - Q_{\text{out}}C_b[\text{HbT}]\text{SO}_{2,\text{out}}) = \sum_{i=1}^M l_i\pi d_i J_i \quad (4.48)$$

and  $M$  is the number of blood vessels inside the tissues. Likewise, (4.48) can be stated as if all the  $\text{O}_2$  is consumed

$$Q[\text{HbT}]_{\text{blood}}(\text{SO}_{2,\text{ti}} - \text{SO}_{2,\text{to}}) = \text{OC}/4 \quad (4.49)$$

For a dynamic case, (4.49) is further written as follows:

$$Q[\text{HbT}]_{\text{blood}}(\text{SO}_{2,\text{ti}} - \text{SO}_{2,\text{to}}) - \text{OC}/4 = \frac{\partial M_{\text{HbO}_2}}{\partial t} \quad (4.50)$$

where  $Q$  is the mean BF for all the blood vessels inside the tissues and is specified as the mean BF of tissues,  $[\text{HbT}]_{\text{blood}}$  is the mean total blood hemoglobin concentration in the blood circulating through the tissues,  $\text{OC}$  is the mean oxygen consumption for the whole tissue volume  $V_{\text{tissue}}$ ,  $M_{\text{HbO}_2}$  is the molar amount of oxygenated hemoglobin inside the measurement volume, and  $\text{SO}_{2,\text{ti}}$ ,  $\text{SO}_{2,\text{to}}$  is the averaged hemoglobin oxygen saturation at the inlet(artery) and outlet(vena) of the tissues, respectively. Moreover, it is noted that the molar amount of oxygenated hemoglobin concentration is expressed as

$$M_{\text{HbO}_2} = \text{SO}_2[\text{HbT}]_{\text{tissue}}V_{\text{tissue}} = [\text{HbO}_2]V_{\text{tissue}} \quad (4.51)$$

Substituting (4.51) into (4.50), we obtain



$$\begin{aligned}
& -\frac{OC}{4V_{\text{tissue}}} + \frac{Q}{V_{\text{tissue}}} [\text{HbT}]_{\text{blood}} (\text{SO}_{2,\text{ti}} - \text{SO}_{2,\text{to}}) \\
& = \text{SO}_2 \frac{d[\text{HbT}]_{\text{tissue}}}{dt} + [\text{HbT}]_{\text{tissue}} \frac{d\text{SO}_2}{dt} = \frac{d[\text{HbO}_2]}{dt}
\end{aligned} \tag{4.52}$$

where  $V_{\text{tissue}}$  is the tissue volume and is assumed constant here, and  $\text{SO}_2$  is the oxygen saturation. If the oxygen supply of tissues depends on the averaged oxygen saturation at the inlet and outlet of the tissues, tissue oxygen saturation should represent the weighted average of the arterial and venous saturation:

$$\text{SO}_2 = f\text{SO}_{2,\text{ti}} + (1-f)\text{SO}_{2,\text{to}} \tag{4.53}$$

Equation (4.53) can be rewritten as follows:

$$\text{SO}_{2,\text{to}} = (\text{SO}_2 - f\text{SO}_{2,\text{ti}})/(1-f) \tag{4.54}$$

Based on (4.54) and (4.52), we get

$$\begin{aligned}
\frac{d\text{SO}_2}{dt} & = -\frac{OC}{4V_{\text{tissue}}[\text{HbT}]} + \frac{Q}{V_{\text{tissue}}[\text{HbT}]} [\text{HbT}]_{\text{blood}} \left( \frac{\text{SO}_{2,\text{ti}}}{1-f} - \frac{\text{SO}_2}{1-f} \right) \\
& \quad - \frac{d[\text{HbT}]}{dt} \frac{\text{SO}_2}{[\text{HbT}]}
\end{aligned} \tag{4.55}$$

Equation (4.55) is the developed mathematical model that connects changes in BF and OC to known HbT and  $\text{SO}_2$  captured by DOT. As such, mean OC and BF can be recovered by fitting (4.55) to time-resolved tissue oxygenation measurements. Equation (4.55) is an ordinary partial differential equation that can be solved iteratively by Runge–Kutta fourth order method coupled with the finite element method [89]. The fitting method is described as follows: with any given initial values for OC and BF within the specified range, this scheme is to optimize the OC and BF parameters based on the solution of (4.55) to reach the following minimized objective function:

$$\text{Min: } \mathbf{F} = \sum_{i=1}^M (\text{SO}_{2i}^m - \text{SO}_{2i}^c)^2 \tag{4.56}$$

in which  $\text{SO}_{2i}^m$  is the measured oxygenation parameter from  $M$  discrete time points,  $\text{SO}_{2i}^c$  is the calculated oxygenation parameter from (4.52) for the same time points. Note the BF and OC are assumed constant during the measurements for the specified time range, due to the need for a sufficient time interval to obtain stable fitting results. Finally, it should be pointed out that Carp et al. also used a model similar to (4.52) to analyze the dynamic response of compressed breast tissues though it seems that their model has no strong theoretical basis [90].

## 4.3 Diffuse Optical Imaging Instrumentation

### 4.3.1 Introduction

According to the type of measured signal, DOT experimental systems are usually classified into three modes: TD, FD, and CW. In the TD mode, the source light is ultra-short-pulsed and the remitted light pulses are broadened. In the FD mode, the source light intensity is amplitude-modulated sinusoidally at typically hundreds of MHz, and in the CW mode, the source light is usually time-invariant. The TD and FD modes are information-rich, but slower in data acquisition and also more expensive than CW mode. It is not clear which method among CW, FD, and TD performs the best. Since CW mode is the most popular and dominant in the field to date, we focus on the introduction of CW imaging systems.

The goal of neuroimaging is to localize or measure the neural activity with different stimuli. We therefore need to use fast CW imaging systems. The most successful series of studies using CW have been performed by the Hitachi Medical Corporation (Tokyo, Japan) using their ETG-100 system [91], which includes eight laser diodes at 780 nm and eight at 830 nm and eight avalanche photodiode lock-in detectors. CW measurements are taken from 24 distinct source–detector pairs held in a regular grid pattern. Typically, two wavelengths at approximately 780 and 830 nm have been chosen, as they lie in the isosbestic point where the absorptions of Hb and HbO<sub>2</sub> are equal. However, recent studies have shown that it is possible to select the optimal wavelengths experimentally or theoretically [73]. It has also been shown that high connector density, for example, 24 sources and 28 detectors embedded in a small probe array, are able to provide the highest spatial resolution of DOT using CW measurements [92].

### 4.3.2 CW DOT Instrumentation

We describe a multi-spectral CW DOT system [93]. Briefly, this DOT system consisted of four main functional units: light generation and delivery unit, optical fiber probe/interface, detection units, and computer system with DAQ (data acquisition board) and Digital I/O (Input/output). CW laser modules (at 8 wavelengths) were used as light sources which delivered light to source optical fibers by means of multichannel optical switches. Optical fiber probe/interface was specially designed for animal study as shown in Fig. 4.3. Light diffused through the rat head was collected and the detected signals were digitalized and stored into the computer. This DOT system was not fast and the data acquisition time was about 1 min per frame ( $6 \times 6$  measurements).

To speed up the data acquisition, a CCD camera-based measurement system was set up for fast neuroimaging and spectroscopy analysis. As shown in Fig. 4.4,



**Fig. 4.3** Photograph of the fiberoptic/rat interface. *D* detection fibers; *S* source fibers. The imaging area is schematically shown as a *rectangle*

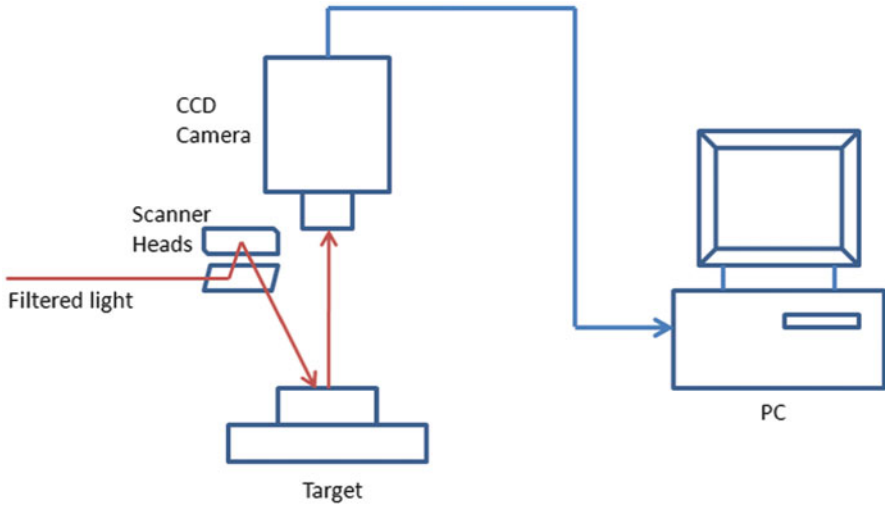


**Fig. 4.4** CCD camera-based imaging setup

filtered light (700 and 750 nm) from a white light source was delivered through 2-axis open frame scanner heads to multiple source points, consequently on surface of the scalp area above the hippocampus. The screening site was imaged onto a CCD camera yielding a raw image of a  $\sim 12 \times 12$  mm area. Data acquisition time was about 750 ms per frame. This system is being used for imaging brain function in small animals.

## 4.4 In Vivo Application

As an example we demonstrate that DOT can be used to visualize the changes in local hemodynamics during seizures. The focal seizure was induced by microinjection 10  $\mu$ L of 1.9 mM GABA<sub>A</sub> antagonist bicuculline methiodide (BMI) into the left parietal neocortex of a male Harlen Sprague–Dawley rat, which was imaged by a multi-spectral DOT system (Fig. 4.3). Functional images were obtained by the finite element-based nonlinear reconstruction algorithms described in Sect. 4.2. A series of dynamic 2D images were obtained to delineate the time course of changes of HbO<sub>2</sub>, Hb, and HbT concentrations in the rat brain during seizure onset. The BMI-induced epileptic foci were localized and observed over time from the images obtained. The results suggest that DOT may be a promising modality for epilepsy imaging due to its ability to localize epileptic foci as well as its potential to map the functional activity in the area of human cerebral cortex in planning of epilepsy surgery.

### 4.4.1 *Animals and the Focal Seizure Model*

Animals used in this study were male Harlen Sprague–Dawley rats, weighing 50–60 g. A total of nine rats were used in this study, of which four were used for DOT and another five were used for electroencephalography (EEG) control study. The rats were housed in pairs in a controlled environment (Temperature:  $21 \pm 1^\circ\text{C}$ ; humidity: 60%; lights on at 8:00 A.M. to 8:00 P.M.; food and water ad lib). The experimental protocols and procedures involving animals and their care were conducted in conformity with NIH and IACUC committee at the University of Florida. Urethane 1 mg/kg was used to anesthetize the rats. A well-established animal model for focal seizures was used. The focal seizure was induced by microinjection GABA<sub>A</sub> antagonist BMI into the left parietal neocortex.

### 4.4.2 *Experiment Method*

As shown in Fig. 4.3, quadrate polycarbonate frames with six holes along each long side was used as an optic fiber holder. Anesthetized rats were mounted on a headset with ear bars and all hair on the scalp was shaved using hair removing lotion before a hole of 1 mm in diameter was drilled through the skull on the left parietal head region. A lab jack was used to adjust the height of the rat's head to a proper position (see Fig. 4.3). The top of the scalp was about 3–4 mm above the plane of the optical fiber array (imaging plane). A piece of clear polyethylene clingwrap was used to cover both the frame structure and the rat's head in order to load Intralipid 0.5% solution as coupling medium for filling the gap between the rat and the

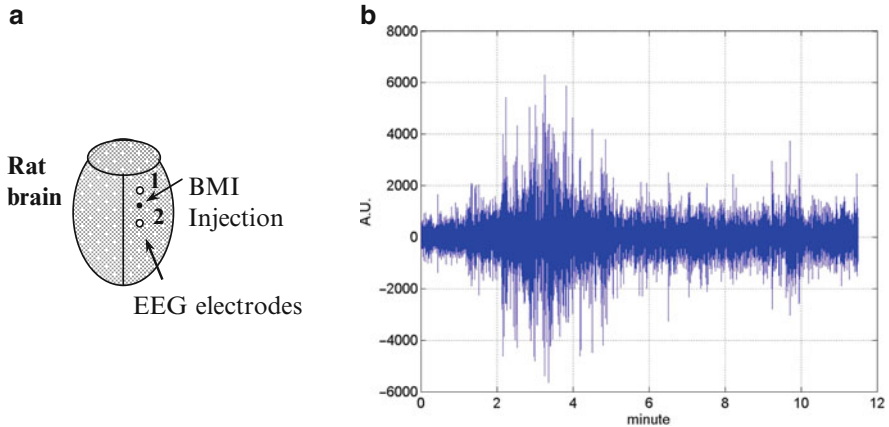


**Fig. 4.5** (a) Locations of BMI injection (*solid dot*) and scalp EEG electrodes (*open circles*). (b) Twelve-minute scalp EEG recording after the injection of BMI on one rat

frame structure. Measurements were made before the BMI injection which was used as calibration data; 10  $\mu\text{L}$  of BMI (1.9 mM) solution was injected by a syringe through the hole prepared before. DOT scans were conducted at several time points (1, 2, 4, 6, 8, and 25 min) after the BMI injection.

### 4.4.3 Electroencephalography Recording

Control experiments were conducted on five rats which were used for EEG recording in order to confirm the occurrence of focal seizure. Scalp EEG recording (two rats) from two electrodes 2.5 mm away from the BMI injection point (as shown in Fig. 4.5a) was recorded. In addition, multichannel EEG (Stellate EEG system) with four screw electrodes (three rats), which were advanced just below the skull and above the dura, was recorded to confirm the localization of seizures. As shown in Fig. 4.5a, two electrodes (#1 and #2) were on the same side of the injection point (left parietal neocortex), while the other two (#3 and #4) were on the opposite side. Distances from the injection point to the four electrodes were 3, 4, 6, and 7 mm, respectively. Rats were anesthetized with urethane (1 mg/kg), and the hairs were shaved with hair removing lotion. A hole of 1 mm in diameter was drilled through the skull on the left parietal head region before rats were put in a stereotaxic apparatus (Kopf), and the electrodes were put on or screwed in. Five-minute stabilized EEG was recorded before 10  $\mu\text{L}$  of BMI (1.9 mM) solution was injected by a syringe through the hole prepared before. Thirty-minute EEG was recorded after the injection of BMI.

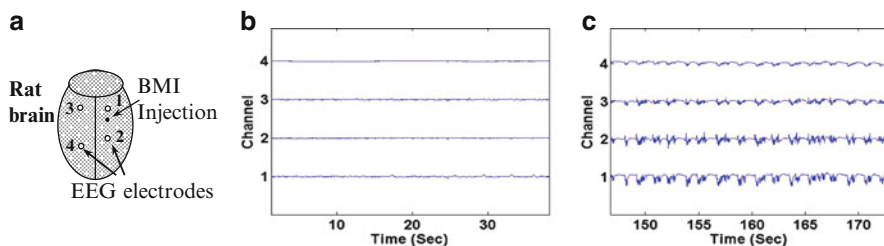


**Fig. 4.6** (a) Locations of BMI injection (*solid dot*) and four EEG electrodes (*open circles*). (b, c) Four-channel EEG recordings from 0 to 40 s and 145 to 175 s on one rat after BMI injection, respectively

#### 4.4.4 Results and Discussion

EEG was used to validate the seizure model. One sample of scalp EEG recording from 0 to 12 min after BMI injection is shown in Fig. 4.5b. Electrographic seizure onset occurs at 2 min following BMI injection as denoted by the rhythmic spiking and twofold increase in EEG amplitude from baseline EEG. Five minutes from the BMI injection time, the EEG postictal spikes are superimposed on the baseline activity. Four-channel EEG recordings from 0 to 40 s and 145 to 175 s on one rat after BMI injection are shown in Figs. 4.6b, c, respectively. Spikes show up in 145–175 s, which delineates the onset of seizures. The difference of amplitude among the signals recorded from four channels can be easily found, suggesting that the onset of seizure is localized.

Images of absolute absorption coefficient ( $\mu_a$ /mm) at three wavelengths (633, 760 and 853 nm) were reconstructed at time points 1, 2, 4, 6, 8, and 25 min. Figure 4.7 presents the HbO<sub>2</sub>, Hb, and HbT images derived from the absorption images at different time points. At the point of injection, localized increase of [HbO<sub>2</sub>], [Hb] and [HbT] (indicated by arrows) can be easily seen.

Here we also show the reconstruction results that demonstrate the feasibility of the recovery of mean BF and OC using the model described in Sect. 4.2.5. To reconstruct BF and OC, the initial parameters were given by: HbT<sub>blood</sub> = 0.72 mM,  $f = 0.2$ , and  $SO_{2,ti} = 0.98$ . The dynamic HbT and  $SO_2$  parameters were first calculated by fitting the reconstructed optical absorption coefficient using Beer's law at wavelengths 633, 760, and 853 nm. In addition, due to the highly nonlinear distribution of dynamic  $SO_2$ , the  $SO_2$  distribution curve was separated into several approximated linear segments to improve the fitting accuracy of BF and OC. The mean BF and OC were fitted for each linear segment based on different initial values of HbT and  $SO_2$ . In this investigation, there were six measurements at 1, 2, 4, 6, 8, and 25 min after seizure onset. For each segment, only two discrete oxygenation measurements were used for the fitting calculation. We specified the fitted mean BF and OC for each segment as the values at the

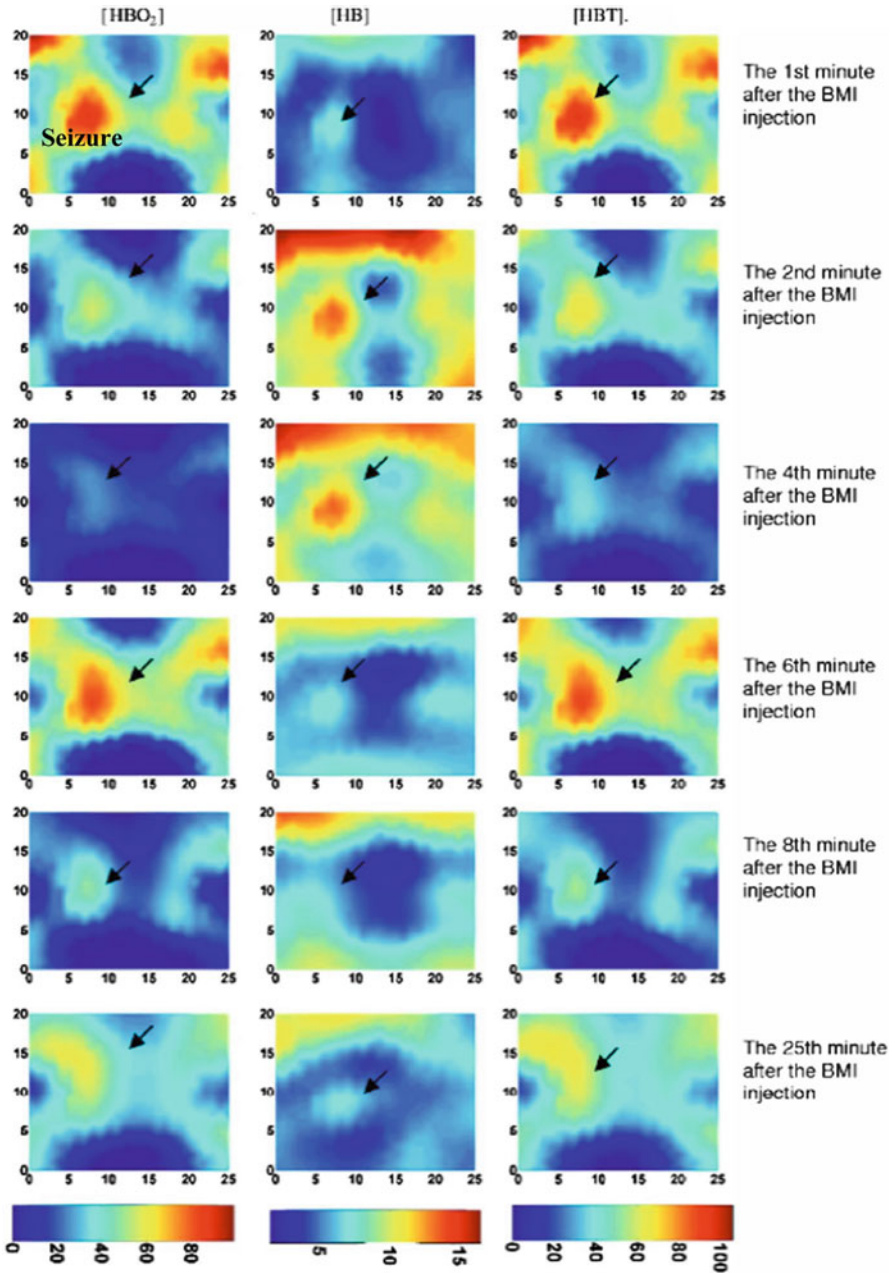
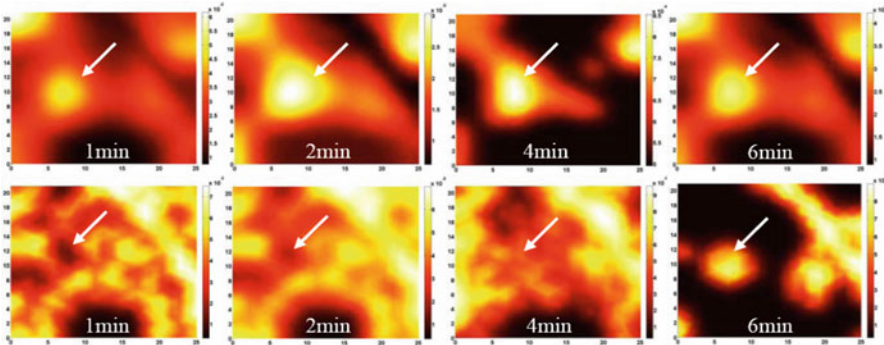
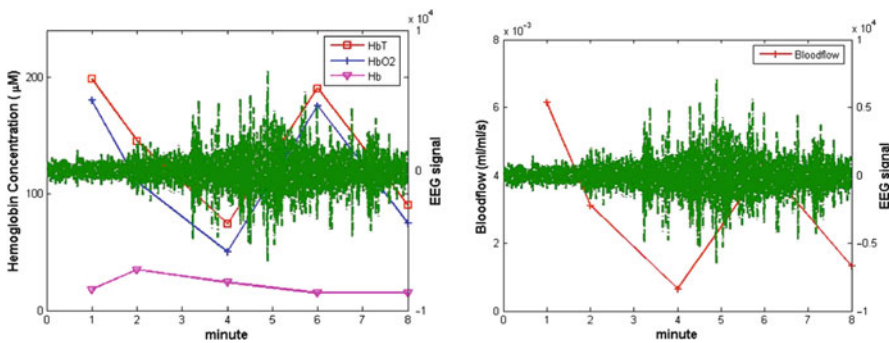


Fig. 4.7 Recovered HbO<sub>2</sub>, Hb, and HbT (μM) images at different time points. *Left:* HbO<sub>2</sub>, *middle:* Hb, *right:* HbT



**Fig. 4.8** Reconstructed volume normalized BF (mL/mL/s) (*top row*), and volume normalized OC ( $\mu\text{mol/mL/s}$ ) (*bottom row*) images at different time points



**Fig. 4.9** The neurovascular and neurometabolic coupling. The *green line* shows the EEG signal

starting point of the segment. For example, we assumed the mean BF and OC fitted between minutes 1 and 2 as the BF and OC at minute 1.

Figure 4.8 presents the reconstructed volume normalized BF and OC images. We see that the seizure is clearly detected with the highest contrast in HbT,  $\text{SO}_2$ , and volume normalized BF. We note that the OC image is not effectively recovered due to the insufficient number of time points used to obtain stable fitting results. Further, it is observed from the peak values of BF shown in Fig. 4.8 that the recovered blood flow values (3.9–36.9 mL/100 mL/min) are in good agreement with the cerebral BF of rats (between 10 and 120 mL/100 mL/min) and humans (20–160 mL/100 mL/min) reported in the literature [94, 95]. The *in vivo* results shown here validate the merits of the mathematical model developed in Sect. 4.2.5.

Figure 4.9 shows that the hallmark of seizure onset correlates with the changes in blood volume, blood oxygenation, and blood flow. As revealed by the quantitative analysis, the auto-regulation of the brain was observed. From Fig. 4.9, we see that HbO<sub>2</sub> and BF oscillate from 1 to 8 min while Hb shows only a flat peak at 2 and 4 min after BMI injection. The fact that average BF, HbO<sub>2</sub> and Hb changed over



time with different patterns indicates the auto-regulation which was the response of the seizure onset. Significant oscillation was found on the change of  $\text{HbO}_2$  and BF instead of Hb which may also be due to auto-regulation. This is because Hb reflects the rate of metabolism while  $\text{HbO}_2$  and BF are highly dependent on the vasomotion which can be contracted or dilated over time through auto-regulation.  $\text{HbO}_2$  and BF in the seizure focus increased with oscillation and reached a peak at 6 min after BMI injection. Hb in the seizure focus increased slowly up to 4 min then decreased 6 min after the injection. These changes in  $\text{HbO}_2$  and BF correlate well with the dynamics captured by the EEG measurements, which reveal the neurovascular and neurometabolic coupling mechanism in neural activity.

## References

1. Yodh A, Chance B (1995) Spectroscopy and imaging with diffusing light. *Phys Today* 48:34–40
2. Gibson A, Dehghani H (2009) Diffuse optical imaging. *Philos Trans R Soc A* 367:3055–3072
3. Jiang H, Iftimia N, Xu Y, Eggert J, Fajardo L, Klove K (2002) Near-infrared optical imaging of the breast with model-based reconstruction. *Acad Radiol* 9:186–194
4. Srinivasan S, Pogue BW, Jiang S, Dehghani H, Kogel C, Soho S, Gibson JJ, Tosteson TD, Poplack SP, Paulsen KD (2003) Interpreting hemoglobin and water concentration oxygen saturation and scattering measured in vivo by near-infrared breast tomography. *Proc Natl Acad Sci U S A* 100:12349–12354
5. Zhu Q, Chen NG, Kurtzman SC (2003) Imaging tumor angiogenesis by use of combined near-infrared diffusive light and ultrasound. *Opt Lett* 28:337–339
6. Durduran T, Choe R, Culver JP, Zubkov L, Holboke MJ, Giammarco J, Chance B, Yodh AG (2002) Bulk optical properties of healthy female breast tissue. *Phys Med Biol* 47:2847–2861
7. Boas DA, Culver JP, Stott JJ, Dunn AK (2002) Three dimensional Monte Carlo code for photon migration through complex heterogeneous media including the adult human head. *Opt Express* 10:159–169
8. Hielscher AH, Klose AD, Scheel AK, Moa-Anderson B, Backhaus M, Netz U, Beuthan J (2004) Sagittal laser optical tomography for imaging of rheumatoid finger joints. *Phys Med Biol* 49:1147–1163
9. Pifferi A, Torricelli A, Taroni P, Bassi A, Chikoidze E, Giambattistelli E, Cubeddu R (2004) Optical biopsy of bone tissue: a step toward the diagnosis of bone pathologies. *J Biomed Opt* 9:474–480
10. Yuan Z, Zhang Q, Jiang HB (2007) 3D diffuse optical tomography imaging of osteoarthritis: initial results in finger joints. *J Biomed Opt* 12:034001
11. Yuan Z, Jiang H (2007) Image reconstruction schemes that combines modified Newton method and efficient initial guess estimate for optical tomography of finger joints. *Appl Opt* 46:2757–2768
12. Ntziachristos V, Bremer C, Graves EE, Ripoll J, Weissleder R (2002) In vivo tomographic imaging of near-infrared fluorescent probes. *Mol Imaging* 1:82–88
13. Cherry SR (2004) In vivo molecular and genomic imaging: new challenges for imaging physics. *Phys Med Biol* 49:R13–R48
14. Davis SC, Dehghani H, Wang J, Jiang S, Pogue BW, Paulsen KD (2007) Image-guided diffuse optical fluorescence tomography implemented with Laplacian-type regularization. *Opt Express* 15:4066–4082
15. Zhou C, Choe R, Shah N, Durduran T, Yu G, Durkin A, Hsiang D, Mehta R, Butler J, Cerussi A, Tromberg BJ, Yodh AG (2007) Diffuse optical monitoring of blood flow and oxygenation

- in human breast cancer during early stages of neoadjuvant chemotherapy. *J Biomed Opt* 12:051903
16. Wilson BC, Patterson MS (1986) The physics of photodynamic therapy. *Phys Med Biol* 31:327–360
  17. Pogue BW, Pitts JD, Mycek MA, Sloboda RD, Wilmot CM, Brandsema JF, O'Hara JA (2001) In vivo NADH fluorescence monitoring as an assay for cellular damage in photodynamic therapy. *Photochem Photobiol* 74:817–824
  18. Cerussi A, Shah N, Hsiang D, Durkin A, Butler J, Tromberg BJ (2006) In vivo absorption, scattering, and physiologic properties of 58 malignant breast tumors determined by broadband diffuse optical spectroscopy. *J Biomed Opt* 11:044005
  19. Dehghani H, Pogue BW, Poplack SP, Paulsen KD (2003) Multiwavelength three-dimensional near-infrared tomography of the breast: initial simulation, phantom, and clinical results. *Appl Opt* 42:135–145
  20. Hebden JC, Yates TD, Gibson A, Everdell N, Arridge SR, Chicken DW, Douek M, Keshtgar MRS (2005) Monitoring recovery after laser surgery of the breast with optical tomography: a case study. *Appl Opt* 44:1898–1904
  21. Yuan Z, Zhang Q, Sobel E, Jiang H (2010) Image-guided optical spectroscopy in diagnosis of osteoarthritis: a clinical study. *Biomed Opt Express* 1:74–86
  22. Iftimia N, Jiang H (2000) Quantitative optical image reconstruction of turbid media by use of direct-current measurements. *Appl Opt* 39:5256–5261
  23. Jiang H, Paulsen KD, Osterberg U, Pogue B, Patterson M (1996) Optical image reconstruction using frequency-domain data: simulations and experiments. *J Opt Soc Am A* 13:253–266
  24. Paulsen KD, Jiang H (1995) Spatially-varying optical property reconstruction using a finite element diffusion equation approximation. *Med Phys* 22:691–701
  25. Tromberg BJ, Pogue BW, Paulson KD, Yodh AG, Boas DA, Cerussi AE (2008) Assessing the future of diffuse optical imaging technologies for breast cancer management. *Med Phys* 35:2443–2452
  26. Carpenter CM, Pogue BW, Jiang S, Dehghani H, Wang X, Paulson KD (2007) Image-guided optical spectroscopy provides molecular-specific information in vivo: MRI-guided spectroscopy of breast cancer hemoglobin, water, and scatter size. *Opt Lett* 32:933–935
  27. Heekeren HR, Obrig H, Wenzel R, Eberle K, Ruben J, Villringer K, Kurth R, Villringer A (1997) Cerebral haemoglobin oxygenation during sustained visual stimulation—a near-infrared spectroscopy study. *Philos Trans R Soc Lond B Biol Sci* 352:743–750
  28. Meek JH, Elwell CE, Khan MJ, Romaya J, Wyatt JS, Delpy DT, Zeki S (1995) Regional changes in cerebral haemodynamics as a result of a visual stimulus measured by near infrared spectroscopy. *Proc R Soc Lond B Biol Sci* 261:351–356
  29. Ruben J, Wenzel R, Obrig H, Villringer K, Bernarding J, Hirth C, Heekeren H, Dirnagl U, Villringer A (1997) Haemoglobin oxygenation changes during visual stimulation in the occipital cortex. *Adv Exp Med Biol* 428:181–187
  30. Sakatani K, Chen S, Lichty W, Zuo H, Wang YP (1999) Cerebral blood oxygenation changes induced by auditory stimulation in newborn infants measured by near infrared spectroscopy. *Early Hum Dev* 55:229–236
  31. Franceschini MA, Fantini S, Thompson JH, Culver JP, Boas DA (2003) Hemodynamic evoked response of the sensorimotor cortex measured non-invasively with near infrared optical imaging. *Psychophysiology* 40:548–560
  32. Colier WN, Quaresima V, Oeseburg B, Ferrari M (1999) Human motor-cortex oxygenation changes induced by cyclic coupled movements of hand and foot. *Exp Brain Res* 129:457–461
  33. Hirth C, Obrig H, Villringer K, Thiel A, Bernarding J, Muhlenthal W, Flor H, Dirnagl U, Villringer A (1996) Non-invasive functional mapping of the human motor cortex using near-infrared spectroscopy. *Neuroreport* 7:1977–1981
  34. Kleinschmidt A, Obrig H, Requardt M, Merboldt KD, Dirnagl U, Villringer A, Frahm J (1996) Simultaneous recording of cerebral blood oxygenation changes during human brain activation

- by magnetic resonance imaging and near-infrared spectroscopy. *J Cereb Blood Flow Metab* 16:817–826
35. Sato H, Takeuchi T, Sakai KL (1999) Temporal cortex activation during speech recognition: an optical topography study. *Cognition* 73:B55–B66
  36. Adelson PD, Nemoto E, Scheuer M, Painter M, Morgan J, Yonas H (1999) Noninvasive continuous monitoring of cerebral oxygenation periodically using near-infrared spectroscopy: a preliminary report. *Epilepsia* 40:1484–1489
  37. Sokol DK, Markand ON, Daly EC, Luerksen TG, Malkoff MD (2000) Near infrared spectroscopy (NIRS) distinguishes seizure types. *Seizure* 9:323–327
  38. Steinhoff BJ, Herrendorf G, Kurth C (1996) Ictal near infrared spectroscopy in temporal lobe epilepsy: a pilot study. *Seizure* 5:97–101
  39. Watanabe E, Maki A, Kawaguchi F, Yamashita Y, Koizumi H, Mayanagi Y (2000) Noninvasive cerebral blood volume measurement during seizures using multichannel near infrared spectroscopic topography. *J Biomed Opt* 5:287–290
  40. Eschweiler GW, Wegerer C, Schlotter W, Spandl C, Stevens A, Bartels M (2000) Left prefrontal activation predicts therapeutic effects of repetitive transcranial magnetic stimulation (rTMS) in major depression. *Psychiatry Res* 99:161–172
  41. Matsuo K, Kato T, Fukuda M, Kato N (2000) Alteration of hemoglobin oxygenation in the frontal region in elderly depressed patients as measured by near-infrared spectroscopy. *J Neuropsychiatry Clin Neurosci* 12:465–471
  42. Okada F, Takahashi N, Tokumitsu Y (1996) Dominance of the nondominant T hemisphere in depression. *J Affect Disord* 37:13–21
  43. Frostig RD, Lieke EE, Tso DY, Grinvald A (1990) Cortical functional architecture and local coupling between neuronal activity and the microcirculation revealed by in vivo high-resolution optical imaging of intrinsic signals. *Proc Natl Acad Sci U S A* 87:6082–6086
  44. Hanlon EB, Itzkan I, Dasari RR, Feld MS, Ferrante RJ, McKee AC, Lathi D, Kowall NW (1999) Near-infrared fluorescence spectroscopy detects Alzheimer's disease in vitro. *Photochem Photobiol* 70:236–242
  45. Hock C, Villringer K, Muller-Spahn F, Hofmann M, Schuh-Hofer S, Heekeren H, Wenzel R, Dirnagl U, Villringer A (1996) Near infrared spectroscopy in the diagnosis of Alzheimer's disease. *Ann N Y Acad Sci* 777:22–29
  46. Chen WG, Li PC, Luo QM, Zeng SQ, Hu B (2000) Hemodynamic assessment of ischemic stroke with near-infrared spectroscopy. *Space Med Med Eng* 13:84–89
  47. Nemoto EM, Yonas H, Kassam A (2000) Clinical experience with cerebral oximetry in stroke and cardiac arrest. *Crit Care Med* 28:1052–1054
  48. Saitou H, Yanagi H, Hara S, Tsuchiya S, Tomura S (2000) Cerebral blood volume and oxygenation among poststroke hemiplegic patients: effects of 13 rehabilitation tasks measured by near-infrared spectroscopy. *Arch Phys Med Rehabil* 81:1348–1356
  49. Vernieri F, Rosato N, Pauri F, Tibuzzi F, Passarelli F, Rossini PM (1999) Near infrared spectroscopy and transcranial Doppler in monohemispheric stroke. *Eur Neurol* 41:159–162
  50. Boas DA, Dale AM, Franceschini MA (2004) Diffuse optical imaging of brain activation: approaches to optimizing imaging sensitivity, resolution and accuracy. *Neuroimage* 23: s275–s288
  51. Taber KH, Hillman E, Hurley R (2010) Optical imaging: a new window to the adult brain. *J Neuropsychiatry Clin Neurosci* 22(4):356–360
  52. Koch SP, Habermehl C, Mehnert J et al (2010) High-resolution optical functional mapping of the human somatosensory cortex. *Front Neuroenergetics* 2:12
  53. White BR, Culver JP (2010) Phase-encoded retinotopy as an evaluation of diffuse optical neuroimaging. *Neuroimage* 49:568–577
  54. White BR, Snyder AZ, Cohen AL et al (2009) Mapping the human brain at rest with diffuse optical tomography. *Conf Proc IEEE Eng Med Biol Soc* 2009:4070–4072

55. White BR, Snyder AZ, Cohen AL, Petersen SE, Raichle ME, Schlaggar BL, Culver JP (2009) Resting-state functional connectivity in the human brain revealed with diffuse optical tomography. *Neuroimage* 47:148–156
56. Arridge SR (1999) Optical tomography in medical imaging. *Inverse Probl* 15:R41–R93
57. Boas DA, Brooks DH, Miller EL, Marzio CAD, Kilmer M, Gaudette RJ, Zhang Q (2001) Imaging the body with diffuse optical tomography. *IEEE Signal Process Mag* 18:57–75
58. Schweiger M, Gibson AP, Arridge S (2003) Computational aspects of diffuse optical tomography. *IEEE Comput Sci Eng* 5:33–41
59. Yamamoto T, Maki A, Kadoya T, Tanikawa Y, Yamada Y, Okada E, Koizumi H (2002) Arranging optical fibres for the spatial resolution improvement of topographical images. *Phys Med Biol* 47:3429–3440
60. Hielscher AH, Alcouffe RE, Barbour RL (1998) Comparison of finite-difference transport and diffusion calculations for photon migration in homogeneous and heterogeneous tissues. *Phys Med Biol* 43:1285–1302
61. Yuan Z, Hu X, Jiang H (2009) A higher-order diffusion model for three-dimensional photon migration and image reconstruction in optical tomography. *Phys Med Biol* 54:65–88
62. Tikhonov A (1977) *Solutions of ill-posed problems*. Wiley, New York
63. Levenberg K (1944) A method for the solution of certain nonlinear problems in least square. *Q Appl Math* 2:164–168
64. Marquardt DW (1963) An algorithm for least-squares estimation of nonlinear parameters. *J Soc Ind Appl Math* 11:431–441
65. Brooksby B, Dehghani H, Pogue B, Paulsen KD (2003) Near Infrared (NIR) tomography breast reconstruction with a prior structural information from MRI: algorithm development reconstruction heterogeneities. *IEEE J Sel Top Quantum Electron* 9:199–209
66. Barbour RL, Graber HL, Chang J, Barbour SS, Koo PC, Aronson R (1995) MRI-guided optical tomography: prospects and computation for a new imaging method. *IEEE Comput Sci Eng* 2:63–77
67. Zhang Q, Brukilacchio TJ, Li A, Scott J, Chaves T, Hillman E, Wu T, Chorlton M, Rafferty E, Moore RH, Kopans DB, Boas DA (2005) Coregistered tomography x-ray and optical breast imaging: initial results. *J Biomed Opt* 10:024033
68. Yuan Z, Jiang H (2010) High resolution x-ray guided three dimensional diffuse optical tomography of joint tissues in hand osteoarthritis: morphological and functional assessments. *Med Phys* 37(8):4343–4354
69. Konecky SD, Wiener R, Choe R, Corlu A, Lee K, Srinivasy SM, Saffer JR, Freifeldery R, Karpys JS, Yodh AG (2006) Diffuse optical tomography and position emission tomography of human breast. *Biomedical Optics Topical Meeting and Tabletop Exhibit, Fort Lauderdale, FL*
70. Yuan Z, Zhang Q, Sobel E, Jiang HB (2008) Tomographic x-ray-guided three-dimensional diffuse optical tomography of osteoarthritis in the finger joints. *J Biomed Opt* 13:044006
71. <http://omlc.ogi.edu/spectra/hemoglobin/index.html>
72. Li A, Zhang Q, Culver JP, Miller E, Boas DA (2004) Reconstructing chromosphere concentrations images directly by continuous-wave diffuse optical tomography. *Opt Lett* 29:256–259
73. Corlu A, Durduran T, Choe R, Schweiger M, Hillman EM, Arridge SR, Yodh AG (2003) Uniqueness and wavelength optimization in continuous-wave multispectral diffuse optical tomography. *Opt Lett* 28:2339–2341
74. Durduran T, Yu G, Burnett M, Detre J, Greenberg J, Wang J, Zhou C, Yodh AG (2004) Diffuse optical measurement of blood flow, blood oxygenation, and metabolism in a human brain during sensorimotor cortex activation. *Opt Lett* 29:1766–1768
75. Dunn A, Devor A, Bolay H, Andermann M, Moskowitz M, Dale A, Boas DA (2003) Simultaneous imaging of total cerebral hemoglobin concentration, oxygenation, and blood flow during functional activation. *Opt Lett* 28:28–30
76. Lauritzen M (2001) Relationship of spikes, synaptic activity, and local changes of cerebral blood flow. *J Cereb Blood Flow Metab* 21:1367–1383

77. Logothetis NK, Pauls J, Augath M, Trinath T, Oeltermann A (2001) Neurophysiological investigation of the basis of the fMRI signal. *Nature* 412:150–157
78. Sakadzic S, Yuan S, Dilekoz E, Ruvinskaya S, Vinogradov A, Ayata C, Boas DA (2009) Simultaneous imaging of cerebral partial pressure of oxygen and blood flow during functional activation and cortical spreading depression. *Appl Opt* 48:169–177
79. Logothetis NK (2008) What we can do and what we cannot do with fMRI. *Nature* 453:869–878
80. Williams DS, Detre JA, Leigh JS, Koretsky AP (1992) Magnetic resonance imaging of perfusion using spin inversion of arterial water. *Proc Natl Acad Sci* 89:212–216
81. Mintun MA, Raichle ME, Martin WR, Herscovitch P (1984) Brain oxygen utilization measured with O-15 radiotracers and positron emission tomography. *J Nucl Med* 25:177–187
82. Patel J, Marks K, Roberts I, Azzopardi D, Edwards AD (1998) Measurement of cerebral blood flow in newborn infants using near infrared spectroscopy with indocyanine green. *Pediatr Res* 43:34–39
83. Fabricius M, Akgoren N, Dirnagl U, Lauritzen M (1997) Laminar analysis of cerebral blood flow in cortex of rats by laser-Doppler flowmetry, a pilot study. *J Cereb Blood Flow Metab* 17:1326–1336
84. Cheung C, Culver JP, Takahashi K, Greenberg JH, Yodanis AG (2001) In vivo cerebrovascular measurement combining diffuse near-infrared absorption and correlation spectroscopies. *Phys Med Biol* 46:2053–2065
85. Kirkham FJ, Padayachee TS, Parsons S, Seargeant LS, House FR, Gosling RG (1986) Transcranial measurement of blood velocities in the basal cerebral arteries using pulsed Doppler ultrasound: velocity as an index of flow. *Ultrasound Med Biol* 12:15–21
86. Themelis G, D'Arceuil H, Diamond SG, Thaker S, Huppert TJ, Boas DA, Franceschini MA (2007) Near-infrared spectroscopy measurement of the pulsatile component of cerebral blood flow and volume from arterial oscillations. *J Biomed Opt* 12:014033
87. Tsai AG, Johnson PC, Intaglietta M (2003) Oxygen gradients in the microcirculation. *Physiol Rev* 83:933–963
88. Sharan M, Vovenko EP, Vadapalli A, Popel AS, Pittman RN (2008) Experimental and theoretical studies of oxygen gradients in rat pial micro vessels. *J Cereb Blood Flow Metab* 28:1597–1604
89. Michael M, William HP, Saul AT, William TV, Brian PF (1986–1992) Numerical recipes in Fortran 77. Cambridge University Press, Cambridge
90. Carp SA, Selb J, Fang Q, Moore R, Kopans DB, Rafferty E, Boas DA (2008) Dynamic functional and mechanical response of breast tissue to compression. *Opt Express* 16:16064–16078
91. Koizumi H, Yamamoto T, Maki A, Yamashita Y, Sato H, Kawaguchi H, Ichikawa N (2003) Optical topography: practical problems and new applications. *Appl Opt* 42:3054–3062
92. Zeff B, White BR, Dehghani H, Schlagger BL, Culver JP (2007) Retinotopic mapping of adult human visual cortex with high-density diffuse optical tomography. *Proc Natl Acad Sci USA* 104:12169–12174
93. Wang Q, Liang X, Zhang Q, Comey P, Jiang H (2008) Visualizing localized dynamic changes during epileptic seizure onset in vivo with diffuse optical tomography. *Med Phys* 35:21–224
94. Hernandez MJ, Brennan RW, Nowman GS (1978) Cerebral blood flow autoregulation in the rats. *Stroke* 9:150–154
95. Sharples PM, Stuart AG, Matthews DS, Aynsley-Green A, Eyre JA (1995) Cerebral blood flow and metabolism in children with severe head injury. Part I: relation to age, Glasgow coma score, outcome, intracranial pressure, and time after injury. *J Neurol Neurosurg Psychiatry* 58:145–152